JOURNAL OF THE AMERICAN CHEMICAL SOCIETY
pubs.acs.org/JACS Article

Downloaded via SHANGHAI ADVANCED RESEARCH INST on January 11, 2021 at 11:31:11 (UTC).
See https://pubs.acs.org/sharingguidelines for options on how to legitimately share published articles.

Intrinsically Active Surface in a Pt/γ-Mo_2N Catalyst for the Water−Gas Shift Reaction: Molybdenum Nitride or Molybdenum Oxide?

Zhe-Shan Zhang,[#] Qiang Fu,[#] Kai Xu, Wei-Wei Wang, Xin-Pu Fu, Xu-Sheng Zheng, Ke Wu, Chao Ma,* Rui Si,* Chun-Jiang Jia,* Ling-Dong Sun, and Chun-Hua Yan

Cite This: *J. Am. Chem. Soc.* 2020, 142, 13362−13371 Read Online

ACCESS | Metrics & More | Article Recommendations | Supporting Information

ABSTRACT: Apart from active metals, supports also contribute significantly to the catalytic performance of supported metal catalysts. On account of the formed strain and defects, the heterostructured surface of the support may play a crucial role to activate the reactant molecules, while it is usually neglected. In this work, the Pt/γ-Mo_2N catalyst was prepared via a facile solution method. This Pt/γ-Mo_2N catalyst showed excellent activity and stability for catalyzing the water−gas shift (WGS) reaction. The reaction rates at 240 °C were 16.5 mol_{CO} $mol_{Pt}^{-1}s^{-1}$ in product-free gas and 5.36 mol_{CO} mol_{Pt}^{-1} s^{-1} in full reformate gas, which were almost 20 times that of the catalysts reported. It is found that the molybdenum species in the surface of the Pt/γ-Mo_2N catalyst is molybdenum oxide as MoO_3. This surface MoO_3 is very easily reduced even at room temperature, and it transformed into highly distorted MoO_x ($2 < x < 3$) in the WGS reaction. The MoO_x on the catalyst surface greatly enhanced the capability of generating active oxygen vacancies to dissociate H_2O molecules, which induced unexpectedly superior catalytic performance. Therefore, the intrinsically active surface in the Pt/γ-Mo_2N catalyst for the WGS reaction was molybdenum oxide as MoO_x ($2 < x < 3$).

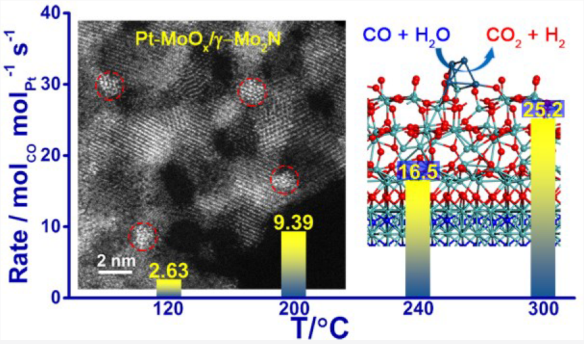

INTRODUCTION

Supported catalysts have been widely used in practical catalysis for their excellent reactivity and low cost.[1−3] In addition to the active metals, supports also contribute a lot to the reactivity of supported metal catalysts.[4,5] Various materials including oxides,[6−8] carbides,[9−11] nitrides,[12] sulfides,[13] and so on have been used as supports to fabricate supported catalysts with remarkable performance in relevant fields. Meanwhile, the studies on the insight of the support effect have attracted considerable attention.[2,4,14−16] Apparently, the surface structure of the supports is one of the most important issues for these studies.[1] As the changes of the catalyst surface probably happen in plenty of catalytic systems, the supports thus will become heterostructured, which results in a fully distinct surface to the bulk in both chemical composition and crystal structure.[17−20] This can inevitably affect the performance of the catalysts and be beneficial to improve the performance of catalysts, with the help of strain and defects generated by the heterostructured interface.[21] However, these structural changes of the support surface are usually too subtle to be detected, for which the crucially positive effect of the heterostructured surface toward catalysts cannot be well cognized. Work on the surface reconstruction of the supports particularly with structural and chemical changes is significantly needed to proceed.

The water−gas shift (WGS) reaction is an important industrial reaction to remove CO from the synthesis gas during the purification of hydrogen.[22,23] This reaction has received increasing interest in the application of hydrogen in proton exchange membrane fuel cells (PEMFCs).[24,25] For the catalyzed WGS reaction, two catalytic mechanisms have been proposed, namely, the redox mechanism and associative mechanism.[26−28] Despite any of the mechanisms, the activation of H_2O is always a critical reaction step that has a significant impact on the reaction rate. Thompson et al.[9] and Ma et al.[11] found that Mo_2C materials exhibit an extraordinary ability to activate H_2O to decompose so that the Mo_2C-supported catalysts show prominent WGS reactivity. Nevertheless, deactivation always occurred during catalytic reactions due to the inevitable oxidation of Mo_2C into inactive MoO_2, which limits further applications.[11,29,30]

According to recent research, surface oxygen vacancy of the catalyst support has been identified as the major site for activating the H_2O molecule.[25,28] Hence, many strategies have

Received: October 15, 2019
Published: July 13, 2020

ACS Publications © 2020 American Chemical Society

https://dx.doi.org/10.1021/jacs.9b11088
J. Am. Chem. Soc. 2020, 142, 13362−13371

been applied to promote the oxygen vacancies of the supports,[31,32] and the most effective one is to increase the intrinsic lattice strain of metal oxides by construction of heterostructured oxide layers on the nonoxide materials.[33,34] For these heterostructured oxide layers, as their activity is significantly affected by the degree of strain, the continuously strained structure built on suitable substrates was essential to avoid deactivation.[35] The γ-Mo_2N that has special crystal and electronic structure was usually used as a support in various catalytic processes but not including the WGS reaction.[12,36−38] Although its surface is partially oxidized during reactions, the γ-Mo_2N was found to maintain a sustained and stable surface structure,[39,40] which makes it a promising candidate as the substrate for the heterostructure.

In this work, to explore and understand the impact of the heterostructured surface of the support, we anchored Pt on the γ-Mo_2N support with surface oxide species to obtain the Pt/γ-Mo_2N catalyst, which exhibited both excellent activity and stability for WGS reaction. We found that, in the WGS reaction, the MoO_x species with plenty of oxygen vacancies on the support surface greatly promoted the dissociation of H_2O molecules to generate surface hydroxyl (−OH) groups that react with the CO adsorbed on the Pt sites. The highly active and stable MoO_x layers on the surface of γ-Mo_2N under the WGS reaction conditions were the consequence of the high stress at the interface between MoO_x and γ-Mo_2N.

■ EXPERIMENTAL SECTION

Catalyst Preparation. *MoO_3 Precursor.* The preparation of the MoO_3 nanobelt precursor was performed by the hydrothermal method, referring to published work,[43] as follows: the triblock copolymer (>99.9%) was evenly dispersed in deionized water. $Na_2MoO_4{\cdot}2H_2O$ (>99.9%) was then dissolved in deionized water and transferred to the above P123 suspension to form a stock solution. Subsequently, the hydrochloric acid was added to the stock solution until the pH value was adjusted to 0.9−1. Then the hydrothermal reaction was performed at 100 °C for 12 h in an oven. After the reaction was completed, the as-obtained product was washed with deionized water and ethanol and then dried at 70 °C. Finally, the as-dried MoO_3 powders were calcined at 400 °C for 4 h in a tube furnace.

γ-Mo_2N Support. The γ-Mo_2N support was prepared under the optimal parameters as follows: the MoO_3 precursor was ground until a particle size of less than 20 mesh and then placed in a tube furnace. High-purity (99.999%) ammonia was introduced as a nitrogen source and a reducing gas at 650 °C for 4 h. After naturally cooling to room temperature (RT), the passivation process was performed in a 1% O_2/Ar mixture gas for 2 h to obtain the stable γ-Mo_2N support.

Pt/γ-Mo_2N Catalyst. The Pt/γ-Mo_2N catalysts were prepared by an ethylene glycol reduction method (EG), referring to published work:[44] the γ-Mo_2N support was dispersed in 200 mL of ethylene glycol with vigorous stirring. Subsequently, an aqueous solution of chloroplatinic acid was added into the stock solution to stir for 10 min, and the solution was then ultrasonically dispersed for 1 h to obtain a well-dispersed slurry. Different pH values (1.5, 5, 8.5, 12) of the slurry were obtained by adding HCl or KOH aqueous solution. The slurry was then refluxed at 140 °C for 2 h. After cooling to RT, the samples were aged at room temperature for 12 h. Finally, the samples were washed with deionized water and absolute ethanol and dried in a vacuum oven at 50 °C for 12 h to obtain Pt/γ-Mo_2N catalysts (0.2 wt % Pt/γ-Mo_2N, 1 wt % Pt/γ-Mo_2N, 2 wt % Pt/γ-Mo_2N) denoted by 0.2Pt−Mo_2N, 1Pt−Mo_2N, and 2Pt−Mo_2N.

The referential preparation methods of the Pt/γ-Mo_2N catalysts include the deposition−precipitation method and impregnation method.

Deposition−Precipitation Method (DP). The γ-Mo_2N support was dispersed in deionized water by vigorous stirring. An appropriate amount of $(NH_4)_2CO_3$ aqueous solution was transferred into the support slurry. Then, the H_2PtCl_6 aqueous solution was added to the slurry. The mixture was aged at room temperature and then washed with deionized water. The obtained catalyst was dried in a vacuum oven at 50 °C for 12 h and denoted by 2Pt−Mo_2N-DP.

Impregnation Method (IMP). The γ-Mo_2N support was dispersed in deionized water by vigorous stirring. Next, the H_2PtCl_6 solution was added to the slurry. The mixture was aged at room temperature and was washed with deionized water. The obtained catalyst was dried in a vacuum oven at 50 °C for 12 h and denoted as 2Pt−Mo_2N-IMP.

Reference Catalysts (Pt-CeO_2 and Pt-TiO_2). A conventional DP method was applied to prepare the reference catalysts: TiO_2 or CeO_2 support was dispersed in deionized water by vigorous stirring. An appropriate amount of $(NH_4)_2CO_3$ aqueous solution was transferred into the support slurry. After the H_2PtCl_6 solution was added to the slurry, the mixture was aged at room temperature and then washed with deionized water. The obtained catalyst was dried in a vacuum oven at 50 °C for 12 h to obtain 2% Pt-CeO_2 and 2% Pt-TiO_2 catalyst (denoted by 2Pt-CeO_2 and 2Pt-TiO_2, respectively).

Characterization of Catalysts. *X-ray Diffraction (XRD).* The *ex situ* and *in situ* X-ray diffraction (XRD) patterns were achieved on a PANalytical B.V. X'pert3 powder diffractometer with Cu K_α radiation (λ = 0.15406 nm) at 40 kV and 40 mA. For the *in situ* XRD experiments, an Anton Paar XRK900 *in situ* chamber was applied. The data were collected from 50 to 400 °C in a 5% H_2/Ar mixture (30 sccm).

Transmission Electron Microscope (TEM). The TEM and high-resolution TEM (HRTEM) images were obtained on JEOL JEM-2800 at 200 kV. The measurements of an aberration-corrected high-angle annular dark-field scanning transmission electron micrograph (HAADF-STEM), STEM energy-dispersive X-ray spectroscopy (EDS), and corresponding electron energy loss spectroscopy (EELS) were performed on a JEOL ARM200F microscope equipped with a probe-forming spherical-aberration corrector. The semi-convergence angle was about 24 mrad, and the inner and outer angles of the detector were 90 and 370 mrad, respectively.

Nitrogen Sorption. The nitrogen sorption measurements were accomplished on a Builder SSA-4200 surface area analyzer to obtain the pore size distribution and surface area of each sample by the BET method as well as the BJH method.

Inductively Coupled Plasma Atomic Emission Spectroscopy (ICP-AES). The ICP-AES measurements were fulfilled on an IRIS Intrepid II XSP instrument (Thermo Electron Corporation).

X-ray Absorption Fine Structure (XAFS). The XAFS spectra of the Pt L_3-edge (E_0 = 11 564 eV) were achieved on the BL14W1 beamline of the Shanghai Synchrotron Radiation Source (SSRF) at 3.5 GeV, using the "top-up" mode with a contrasting 260 mA current. The XAFS data were gathered under fluorescence mode by a seven-element Ge solid-state detector. The energy was calibrated according to the absorption edge of Pt foil, and data extraction and profile fitting were performed by the Athena and Artemis programs.

X-ray Photoelectron Spectroscopy (XPS). XPS measurements were accomplished on an Axis Ultra XPS spectrometer (Kratos, U.K.) at a K_α-ray of a 225 W Al target. The correction was performed with a peak at C 1s at 284.8 eV. Besides, Mo 3d XPS spectra for a 0.2Pt−Mo_2N catalyst with synchrotron radiation were conducted by an X-ray source with different energies of 400, 800, and 1253.6 eV.

Ex/In Situ Raman Tests. The *ex situ* and *in situ* Raman spectroscopy tests were performed on a microlaser confocal Raman spectrometer of model LabRAM HR800 (HORIBA JOBIN YVON corporation). The wavelength of laser excitation was 633 nm. The samples (0.2Pt−Mo_2N or Mo_2N support) were sealed in the *in situ* chamber for *in situ* Raman tests. The programs of *in situ* tests were as follows:

(i) Room-temperature treatments. The 0.2Pt−Mo_2N and γ-Mo_2N supports were purged by air (21% O_2/N_2), Ar (99.999%), air, and 5% H_2/Ar subsequently at RT, each gas for 10 min.

(ii) Reduction and WGS reaction treatments. The samples were reduced at 300 °C in 5% H_2/Ar for 30 min. Then, the signal of the reduced sample was detected by switching to Ar at 300 °C to avoid fluorescence interference. After the reduction, the temperature was cooled to 150 °C to introduce the WGS reaction gas (2% CO/3% H_2O/N_2) to treat the samples for 30 min.

(iii) Renitridation treatments by NH_3. The catalysts were purged with Ar (99.999%) for 30 min at RT. Then the gas flow was changed to 10% NH_3/Ar at RT, and the temperature was increased to 500 °C to renitride the samples for 2 h. After the renitridation, the gas flow was shifted to the WGS reaction gas at 150 °C and maintained for 1 h.

(iv) Oxidation treatments by H_2O. The samples were purged by 3% H_2O/N_2 at room temperature and then heated to 300 °C for 30 min in 3% H_2O/N_2. After that, the temperature was cooled to RT, and the gas flow was changed to Ar.

The gas flow rates for the above tests were all 10 mL/min, and the Raman spectra were collected after each gas or temperature was changed. The scanning range was 100−1200 cm^{-1}.

Temperature-Programmed Reduction by CO (CO-TPR). The CO-TPR tests were conducted on an in-line mass spectrometer (LC-D200M, TILON). The 100 mg samples were activated in Ar (30 sccm) at 400 °C for 30 min. When the temperature was cooled to RT, the gas flow was changed to He for 0.5 h and then changed to 2% CO/He. After pretreatments, the temperature was increased to 400 °C to perform the CO-TPR.

Temperature-Programmed Desorption of CO (CO-TPD). The CO-TPD tests were also performed on the mentioned mass spectrometer. The 300 mg samples were activated at 5% H_2/Ar (30 sccm) at 300 °C for 30 min, and the impurities on the surface at 600 °C for 30 min in pure He were removed. After pretreatments, the samples were purged by 2% CO/He for 30 min to adsorb the CO. Then, the gas flow was switched to pure He for 30 min at RT, and the temperature was increased to 400 °C to perform the process of CO-TPD.

Temperature-Programed Surface Reaction of CO (CO-TPSR). The CO-TPSR test was also performed on the in-line mass spectrometer. Before the CO-TPSR, the catalysts were activated by 5% H_2/Ar (30 sccm) at 300 °C for 30 min. After that, the samples were prehydroxylated with 3% H_2O/He (30 sccm) for 30 min and then purged by pure He gas (50 sccm) at 200 °C for another 30 min to clear the physically adsorbed H_2O molecules. To eliminate the influence of dead volume during operation, a six-way valve was applied to switch the various gas flows, and therefore the catalysts cannot be exposed to air after the activation step. Finally, after activation and adsorption of −OH, the gas flow was changed to 2% CO/He (30 sccm) for 20 min at 25 °C, and then the catalysts were heated to 400 °C (5 °C/min) to perform the surface reaction with CO molecules.

Catalytic and Kinetic Tests. *Catalytic Performance.* The WGS reactivity of Pt/γ-Mo_2N samples was evaluated on a fixed-bed reactor of atmospheric pressure. Twenty-five mg sieved catalysts (20−40 mesh) were mixed with SiO_2 powders and placed in a stainless-steel tube with an inner diameter of 8 mm. The WGS reactivity of Pt/γ-Mo_2N catalysts was tested in product-free gas (2% CO/10% H_2O/N_2), and the total gas hourly space velocity (GHSV) was 168 000 mL h^{-1} g^{-1}. Before the test, the catalysts were pretreated in 5% H_2/Ar at 300 °C for 30 min. Typically, the catalytic tests were performed from 120 to 300 °C with 30 °C per step. The stability tests were performed with GHSV of 252 000 mL h^{-1} g^{-1} at 200 °C for over 94 h and down to 120 °C for another 94 h. The outlet gas compositions of CO and CO_2 were analyzed by an infrared gas analyzer (Gasboard-3100, Wuhan Sifang Corporation).

The catalytic performance of the catalyst in the full reformate gas was also evaluated with the feed composition of the 7% CO/22% H_2/10% CO_2/15% H_2O/N_2 balance. Besides, the GHSVs of the tests of activity and long-term stability were 56 000 mL h^{-1} g^{-1} and 84 000 mL h^{-1} g^{-1}, respectively.

Kinetics Tests. An appropriate amount (5−10 mg) of Pt/γ-Mo_2N catalysts, as well as reference catalysts, was mixed with SiO_2 powders. When mass transfer limitation was eliminated with the GHSV above 840 000 mL h^{-1} g^{-1}, the E_a values were achieved after experiments by changing temperature and gas flow rate, along with conversions being limited to between 10% and 15% (10% < Conv._{CO} < 15%) at the same time. Herein, the specific reaction rates (r) of catalysts can be calculated by the formula:

$$r_{Pt} = \text{GHSV}_{CO} \times \text{Conv.}_{CO} / n_{Pt} \quad (1)$$

To determine the CO and H_2O reaction orders, the partial pressures of CO and H_2O were changed from 3% to 18% and from 4% to 20% during measurements, respectively. Besides, the WGS conversion was limited to 10% with the GHSV above 1 000 000 mL h^{-1} g^{-1}.

For a more objective evaluation of catalysts, the tests of kinetics of catalysts were also performed under full reformate gas with feed composition of 7% CO/22% H_2/10% CO_2/15% H_2O/N_2 (10% < Conv._{CO} < 15%).

Theoretical Calculations and Studies. The methods of simulations are displayed in the Supporting Information.

■ RESULTS AND DISCUSSION

Preparation and Catalytic Performance Evaluation of Catalysts. The γ-Mo_2N support was prepared by a temperature-programmed nitridation of MoO_3 nanobelts in NH_3. After that, a mild passivation process was adopted to protect the freshly made γ-Mo_2N, the structure and morphology of which are shown in Figure 1. TEM and HRTEM images indicate that the γ-Mo_2N support is a porous nanosheet constructed of nanoparticles smaller than 10 nm (Figure 1, a and c). From the XRD pattern (Figure 1e), we can see that the

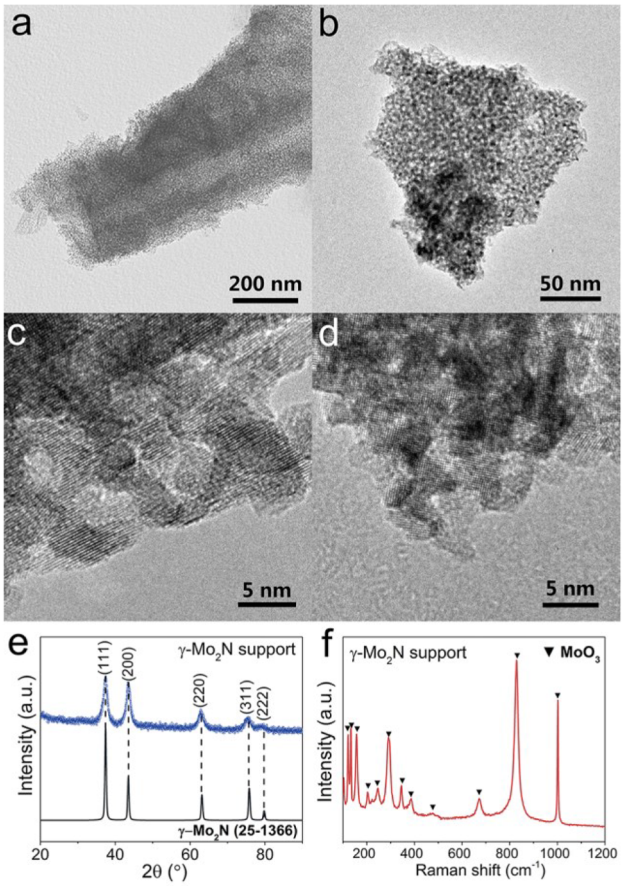

Figure 1. Characterization of the prepared γ-Mo_2N support and Pt/γ-Mo_2N samples. (a) TEM image, (c) HRTEM image, (e) XRD pattern, and (f) Raman spectrum of the prepared γ-Mo_2N support. (b) TEM and (d) HRTEM images of the fresh 0.2Pt−Mo_2N sample.

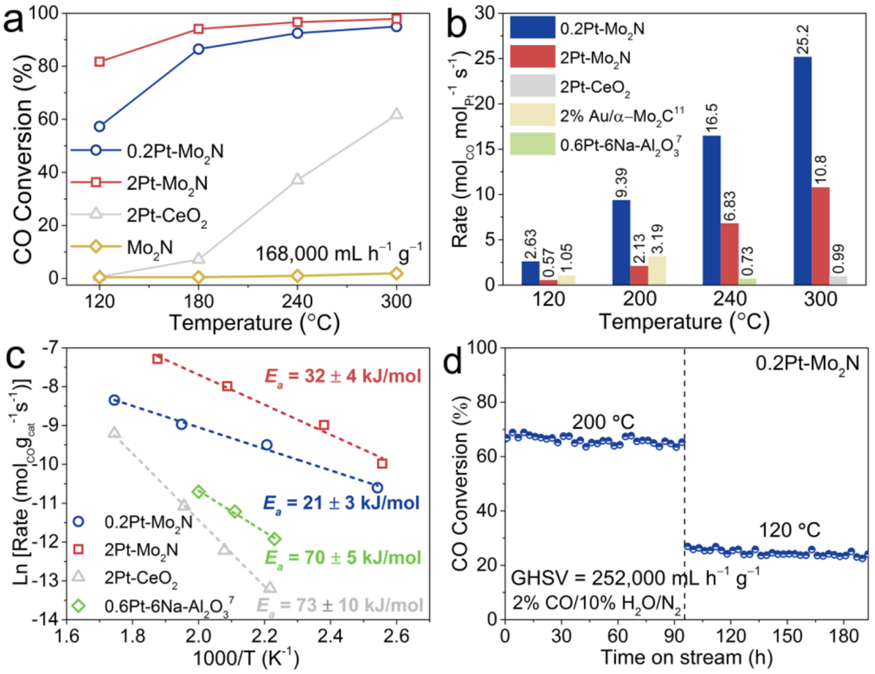

Figure 2. Catalytic performance of the 0.2Pt−Mo_2N and 2Pt−Mo_2N catalysts. (a) CO conversion for the WGS reaction of 0.2Pt−Mo_2N and reference catalysts under product-free gas (test conditions: 2% CO/10% H_2O/N_2, GHSV = 168 000 mL h^{-1} g^{-1}). (b) Catalytic reaction rates and (c) apparent activation energy E_a of different catalysts under product-free gas (test conditions: 2% CO/10% H_2O/N_2,10% < $Conv._{CO}$ < 15%). (d) Long-term catalytic test of 0.2Pt−Mo_2N catalyst (test conditions: 2% CO/10% H_2O/N_2, GHSV = 252 000 mL h^{-1} g^{-1}, 200 or 120 °C).

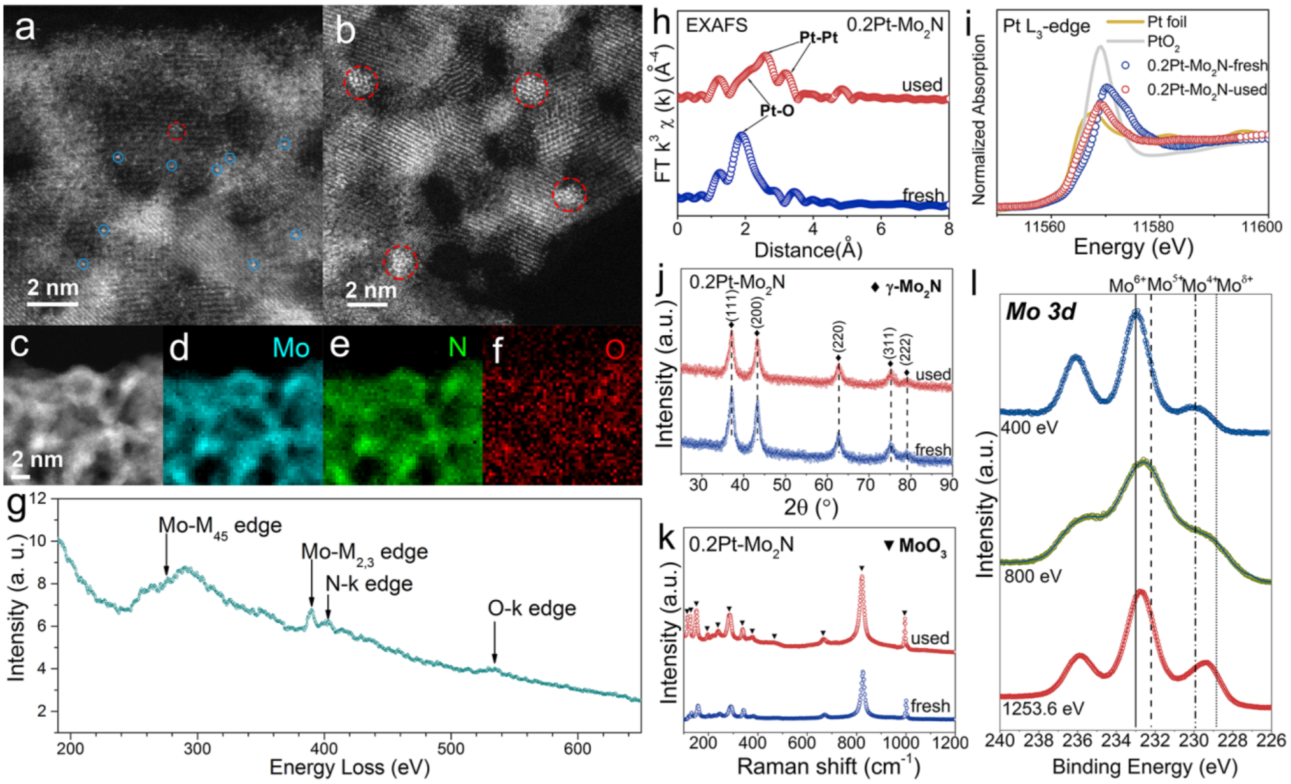

Figure 3. Structural characterization of the 0.2Pt−Mo_2N catalyst. STEM image of the (a) fresh 0.2Pt−Mo_2N and (b) the catalyst after stability tests. Elemental analysis of the 0.2Pt−Mo_2N catalyst after the WGS reaction via (c−f) STEM-EDS and the (g) corresponding EELS results. (h) EXAFS spectra, (i) XANES spectra, (g) XRD patterns, and (k) Raman spectra of the 0.2Pt−Mo_2N catalyst before and after WGS reaction. (l) Mo 3d XPS spectra of the fresh 0.2Pt−Mo_2N catalyst with synchrotron radiation of different X-ray energy.

support is γ-Mo_2N without any other phase, while the Raman results indicate that MoO_3 is formed on the surface of the γ-Mo_2N support after the passivation process (Figure 1f). Since there is no MoO_3 detected by XRD, the amount of the surface

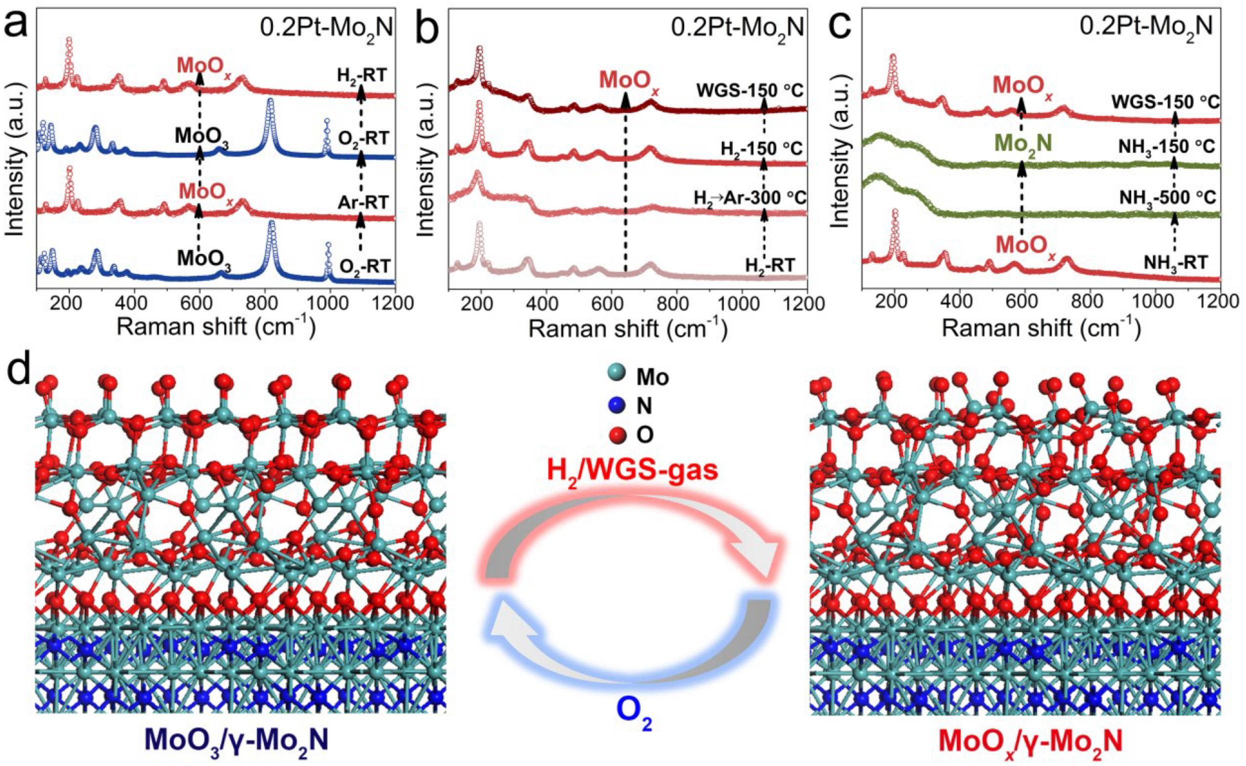

Figure 4. *In situ* characterization and simulated structure model of the 0.2Pt−Mo_2N catalyst with different treatment programs. (a) *In situ* Raman spectra in treatment of switchover of O_2, Ar, and H_2 at RT (21% O_2/N_2, pure Ar, and 5% H_2/Ar). (b) *In situ* Raman spectra in the reduction (5% H_2/Ar → Ar, 300 °C) and WGS reaction treatment process (2% CO/3% H_2O/N_2, 150 °C). (c) *In situ* Raman spectra in the renitridation (10% NH_3/Ar, 500 and 150 °C) and WGS reaction treatment process (2% CO/3% H_2O/N_2, 150 °C). (d) Schematic diagram of structure transformation of the surface oxide layers in the form of MoO_3/γ-Mo_2N and MoO_x/γ-Mo_2N for the 0.2Pt−Mo_2N catalyst. The teal, blue, and red spheres represent the Mo, N, and O atoms, respectively.

MoO_3 on the γ-Mo_2N must be very low. To load Pt components, we adopted several facile solution methods, including EG, IMP, and DP methods, to obtain a series of Pt/γ-Mo_2N catalysts, not changing the basic morphology of the γ-Mo_2N support (Figure 1, b and d). To compare the performance of the catalyst, 2Pt-CeO_2 and 2Pt-TiO_2 catalysts were also prepared as reference catalysts.

The performance for the WGS reaction on the Pt/γ-Mo_2N catalysts was evaluated in product-free gas and full reformate gas. In Figure S1, according to the series of contrast experiments, the Pt/γ-Mo_2N catalysts prepared by the EG method presented the best WGS reactivity, and these catalysts only showed remarkable activity when they were activated by the H_2 (Figure S1). After further optimizing the preparation and pretreatment conditions, we found that the samples with loading of 2 wt % Pt (2Pt−Mo_2N) and 0.2 wt % Pt (0.2Pt−Mo_2N) both show excellent activity. In product-free gas with a high space velocity of 168 000 mL h^{-1} g^{-1}, the CO conversions ($Conv._{CO}$) increase with the temperature from 58% at 120 °C to 94% at 300 °C and 81% at 120 °C to 99% at 300 °C for the 0.2Pt−Mo_2N and 2Pt−Mo_2N catalysts, respectively (Figure 2a), which are much higher than those of reference catalysts. Impressively, the specific rates of Pt on 0.2Pt−Mo_2N reach 2.63, 9.39, 16.5, and 25.2 mol_{CO} mol_{Pt}^{-1} s^{-1} at 120, 200, 240, and 300 °C, respectively, which are almost three times higher than the best Pt catalyst[9] and four times higher than the best Au catalyst[11] at the same temperature ever reported (Figure 2b, Figure S2, and Table S1). Furthermore, we performed the kinetic tests to reveal the cause of superior reactivity on the 0.2Pt−Mo_2N. As shown in Figure 2c, the apparent activation energy E_a of the 0.2Pt−Mo_2N sample is only 21 kJ/mol, significantly lower than that of the 2Pt-CeO_2 (73 kJ/mol), 2Pt-TiO_2 (61 kJ/mol, Figure S3), and other reference catalysts in the literature.[7] This suggests that the WGS reaction is much easier to take place on 0.2Pt−Mo_2N than on the metal oxide-supported Pt catalysts previously reported. Furthermore, we have accomplished additional tests by varying the flow rate and particle size to exclude the influence of the external diffusion and internal diffusion, indicating that the results of the reaction rate, activation energy, and reaction order were obtained from the kinetically controlled region (Figure S4). To evaluate the long-term stability of 0.2Pt−Mo_2N, the catalytic test was continuously carried out at 200 and 120 °C for a total of 192 h under the ultrahigh space velocity of 252 000 mL h^{-1} g^{-1}. The conversions of CO can be stably maintained at 65% and 25%, respectively, without any observable deactivation during the whole test (Figure 2d). In the full reformate gas, the activity of 0.2Pt−Mo_2N decreased considerably due to the presence of H_2 and CO_2 reaction products, but the long-term stability still remained rather strong (Figure S2d). Therefore, the structure and active species of the 0.2Pt−Mo2N catalyst were further investigated to clarify the source of high performance for the WGS reaction.

Structure Characterization of Catalysts. As shown in Figure 3, multiple characterization methods were applied to investigate the structure of the catalysts. HADDF-STEM and extended X-ray absorption fine structure (EXAFS) tests were conducted to determine the specific structure of the Pt species

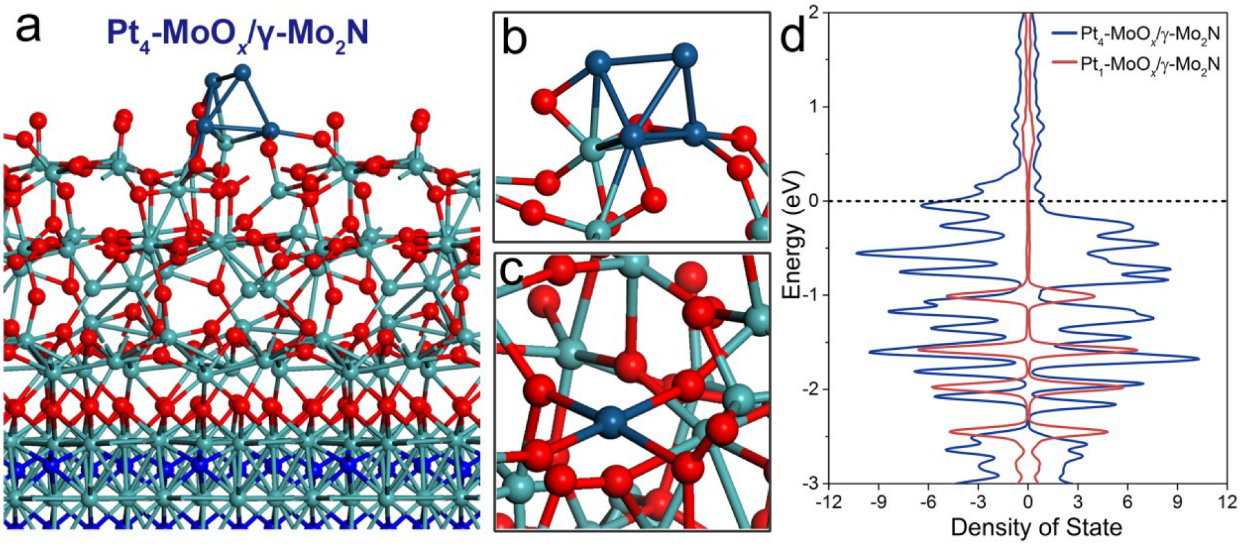

Figure 5. Configuration of the Pt cluster and the Pt single atom on MoO_x/γ-Mo_2N. (a,b) Pt_4−MoO_x/γ-Mo_2N model and (c) Pt_1−MoO_x/γ-Mo_2N model. (d) Calculated electronic density of states (DOS) of the Pt d orbitals for both Pt_4−MoO_x (blue line) and Pt_1−MoO_x (red line). The Fermi level is set to zero. The teal, dark-blue, gray, red, and white spheres represent the Mo, Pt, C, O, and H atoms, respectively.

on the 0.2Pt−Mo_2N catalyst. The STEM images show that the Pt in the catalyst before the WGS reaction test are atomically dispersed species. After the long-term stability test, the Pt species agglomerate into clusters with size under 2 nm (Figure 3a,b). As shown in the EXAFS spectra, only the Pt−O coordination shell, without an observable Pt−Pt metallic bond, appears in the R-space EXAFS spectrum before WGS reaction (Figure 3h). Besides, the metallic Pt−Pt shell of 0.2Pt−Mo_2N emerges after the activity and stability test, while the Pt−O contribution is significantly reduced. Thus, it was concluded that the oxidized Pt species are partially converted to the metallic Pt clusters after WGS reaction, additionally with the evidence from the X-ray absorption near-edge spectroscopy (XANES) characterization (Figure 3i) as well as the XPS results (Figure S5). As for the 2Pt−Mo_2N catalyst, STEM images and STEM-EDS show that there are predominantly Pt clusters and single atoms in the 2Pt−Mo_2N catalyst before the WGS reaction, whereas much more Pt particles appeared after the WGS reactions, in line with the results of EXAFS and XPS (Figures S6−S9 and Table S2), which may lead to the lower specific rates than that of 0.2Pt−Mo_2N samples.

The XRD results show that the bulk structures of the catalyst before and after the reaction are both γ-Mo_2N (JCPDS card no. 25-1365), indicating that the host part of the γ-Mo_2N support is stable during the WGS reaction processes (Figure 3j). Besides, the results of TEM, XRD, and BET also show that the γ-Mo_2N support of the catalyst can maintain the structure, morphology, and specific surface area of the nanosheets after WGS reaction (Figures S10−S13 and Table S3). On the basis of *ex situ* Raman results, the MoO_3 layers are formed on the surface of the Pt−Mo_2N catalyst before and after WGS reaction, which is identical with the pristine γ-Mo_2N support (Figure 3k). In addition, the results of STEM-EDS and EELS analysis clearly show that the uniformly dispersed oxygen element appears on the surface of the 0.2Pt−Mo_2N catalyst after the WGS reaction, attributed to the surface oxide layer of the catalyst (Figure 3c−g).

In Figure 3l, XPS spectra excited by X-ray of different energies showed different chemical valences of the Mo. The spectra of the innermost Mo species and middle Mo species detected by an X-ray of 1253.6 and 800 eV both exhibit the distribution of $Mo^{\delta+}$ ($2 < \delta < 3$), Mo^{4+}, Mo^{5+}, and Mo^{6+}, despite the difference of relative amounts of each species. However, the spectra of the outermost Mo species with X-ray of 400 eV only show the Mo^{4+}, Mo^{5+}, and Mo^{6+}. Thus, we found that the XPS spectra with multiple energies of the X-ray source show differential core spectra of Mo at different depths of the γ-Mo_2N support, which indicates that the Mo species on the surface of the γ-Mo_2N support present higher valence states than that of the inner γ-Mo_2N.

Clarification of Surface Structure. To get insight into the surface structure of the catalyst, we carried out *in situ* Raman experiments with different treatment programs (Figure 4). First, when the atmosphere was switched between 1% O_2/Ar and 5% H_2/Ar (Figure 4a), the phase of the surface transformed between MoO_3 and MoO_x ($2< x < 3$) at room temperature.[41,42] This result means that the surface species on the γ-Mo_2N substrate were very sensitive to the external O_2 partial pressure, and the presence of oxygen was necessary to maintain the fully oxidized MoO_3 structure. Besides, we also performed *in situ* Raman tests under the WGS reaction conditions, which demonstrated that the surface Mo species of the catalyst is MoO_x whether after the pretreatment in H_2 at 300 °C or in the WGS reaction atmosphere at 150 °C (Figure 4b). Furthermore, the MoO_x can be completely removed in NH_3 at 500 °C, but it was recovered after the WGS reactant gas was switched on (Figure 4c). Thus, according to the evidence from *in situ* Raman tests, we believed that the surface of the γ-Mo_2N support of the catalyst is MoO_x, which is induced to form a heterostructured MoO_x/γ-Mo_2N during WGS reaction, regardless of activation by H_2 or NH_3. The schematic diagram shows the whole transformation process of the surface structure (Figure 4d). Moreover, the surface structure of pristine γ-Mo_2N supports is also sensitive to the O_2 partial pressure, as shown in Figure S14.

We used DFT simulations to illustrate the properties of the MoO_x species generated on the γ-Mo_2N substrate. The corresponding model for the heterostructured MoO_3/γ-

Mo_2N (111) system was shown in Figure S15a,b. We found that the MoO_3 thin layers on the γ-Mo_2N exhibit a very small formation energy of oxygen vacancies, which is only 0.35 eV under a low O_2 partial pressure of 10^{-6} atm. Such low formation energy is consistent with the observed stoichiometry of MoO_x ($2 < x < 3$) during the Raman tests at room temperature. Further analysis revealed that the low formation energy is not due to the size effect caused by the low thickness of the MoO_3 thin layers but comes from the stress induced by the mismatch of lattices between MoO_3 and γ-Mo_2N. Specifically, our calculations on a pure MoO_3 thin layer show that the formation energy of oxygen vacancies is as high as 1.89 eV using a strainless model but remarkably decreases to 0.17 eV once the same amount of stress is exerted as that in the heterostructured MoO_3/γ-Mo_2N(111) system. More interestingly, to achieve such low formation energy, the stress should not be applied in an arbitrary way but must be exerted in a specific pattern. As shown in Figure S15c−f, stretching the two base vectors of the MoO_3 plane cannot largely affect the formation energy, while increasing the angle between the two vectors can significantly reduce such values. In this sense, compared to traditional supports, the heterostructured MoO_x/γ-Mo_2N provides a natural and smart way to lower the formation energy of oxygen vacancies, which can bring improvement in catalytic properties toward the WGS reaction.

In order to clarify the effects of Pt species on the 0.2Pt−Mo_2N catalyst for WGS reaction, the simulation models for the Pt_4−MoO_x/γ-Mo_2N (Figure 5a,b) and Pt_1−MoO_x/γ-Mo_2N (Figure 5c) systems were constructed on the basis of the experimental results of the EXAFS spectra and HADDF-STEM images. The two types of Pt species exhibit very different interaction strengths with the adsorbate, which can be interpreted from their distinct electronic structures. In Figure 5d, we present the calculated density of state (DOS) of the Pt *d* orbitals. One can see that for the Pt_1−MoO_x/γ-Mo_2N model the distribution of the *d* states in the energy space (red line) is narrow and mainly located in regions that are far from the Fermi level, while for the Pt_4−MoO_x/γ-Mo_2N system, the corresponding *d* states (blue line) are more extended and still possess a large contribution near the Fermi level. It means that the latter can bond and interact more effectively with the adsorbates such as the produced hydrogen atoms and therefore are expected to play a more active role in the catalytic reactions.

WGS Mechanism Investigation. We further performed the kinetic tests to study the relationship between the adsorption of reactants and reaction rates. The reaction orders of CO and H_2O were measured at different temperatures (Figure 6). As shown in Figure 6a, the reaction orders of CO are −0.24 at 120 °C, 0.13 at 180 °C, and 0.12 at 240 °C, which suggests the sufficient adsorption of CO in the WGS reaction. However, in Figure 6b, the reaction orders of H_2O are 1.1 at 120 °C, 0.94 at 180 °C, and 0.61 at 240 °C, proving that the adsorption of H_2O on the catalyst is insufficient. Furthermore, obviously, the reaction orders of H_2O decrease with increasing temperature. It indicates that as the temperature increases the ability of adsorption and dissociation of H_2O molecules is enhanced over Pt/γ-Mo_2N catalysts, which releases the shortage of the H_2O for WGS reaction. Therefore, toward the WGS reactivity of Pt/γ-Mo_2N catalysts, one of the most crucial properties is the capability of H_2O adsorption and dissociation. Based on the aforementioned results of DFT simulations, oxygen vacancies can easily be formed within the MoO_3 thin layers on γ-Mo_2N. We thus investigated the dissociation of H_2O molecules at such surface oxygen vacancy sites. It is found that the thermodynamic energy cost to form hydroxyls (−OH) is only 0.29 eV (Figure S16), confirming that the dissociation of H_2O is relatively easy to fulfill on the special surface structure of MoO_x/γ-Mo_2N. A factor that may affect the reaction order of water is the coadsorption of the produced hydrogen atoms on Pt clusters. Since the H_2 desorption via a combination of two H atoms on Pt is an endothermic process, the produced hydrogen atoms will stay for a certain time on the interfacial Pt atoms. The presence of such hydrogen atoms will hinder the adsorption and the subsequent dissociation of incoming water molecules, which increases the reaction order of water. Such a factor well explains the dependence of the reaction order with the reaction temperature in Figure 6b. With the increase of the temperature, the hydrogen desorption becomes faster and thus brings about easier adsorption of the water molecules.

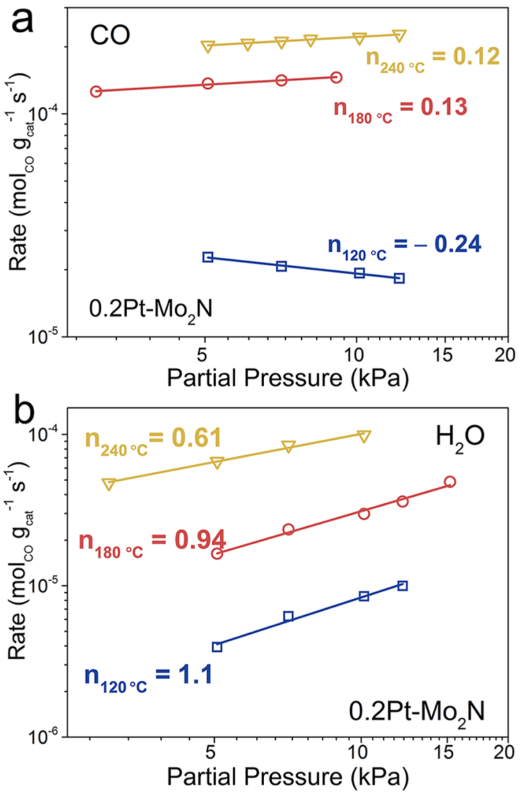

Figure 6. Further study of the WGS reaction kinetics. Kinetic order of (a) CO and (b) H_2O on the 0.2Pt−Mo_2N catalyst at 120, 180, and 240 °C.

To determine the WGS reaction mechanism on Pt/γ-Mo_2N catalysts, we have designed a two-step CO-TPSR experiment. As shown in Figure 7a, after activation, adsorption of −OH, and removal of surface H_2O molecules, the CO was subsequently introduced to adsorb and react on the catalyst. The coproduction of CO_2 and H_2 ($CO_2/H_2 = 2$) at temperatures higher than 100 °C is attributed to the reaction of surface −OH and CO ($CO + OH = CO_2 + 1/2H_2$). Besides, the initial formation of CO_2 at low temperature is attributed to the reaction between CO and residually active O* species or the terminal −OH groups, which contributes barely to the WGS reactivity (Figure S17).[28] To clarify the potential redox pathway, the H_2O-TPSR and He-TPSR have been

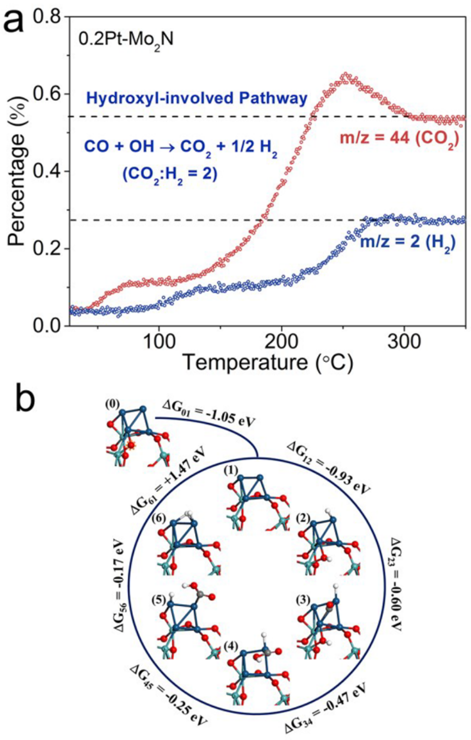

Figure 7. Mechanism study of the WGS reaction on the 0.2Pt−Mo_2N catalyst. (a) CO-TPSR of the 0.2Pt−Mo_2N catalyst. (b) Proposed WGS reaction pathway on the 0.2Pt−Mo_2N catalyst. The teal, dark-blue, gray, red, and white spheres represent the Mo, Pt, C, O, and H atoms, respectively.

performed, and the results reveal that neither the H_2O molecules nor surface −OH can be decomposed to produce H_2 without the presence of CO (Figure S18). Therefore, the reaction pathway in the WGS reaction over the Pt/γ-Mo_2N catalysts is that CO reacts with surface −OH rather than with O* species. Based on these results, it can be revealed that the WGS reaction on Pt/γ-Mo_2N does not follow the redox mechanism but follows the associative mechanism involving −OH according to the published literature.[26] Besides, results from our first-principles simulations do not support the redox mechanism either, with more detailed results presented in the Supporting Information (Figure S19). Additionally, the proposed entire reaction pathway on the established Pt_4−MoO_x/γ-Mo_2N was schematically shown in Figure 7b. The hydrogen-containing active intermediates of the carboxylate (−COOH) are more preferable to generate in the pathway. For this pathway, upon the deposition of Pt, CO can react with the interfacial hydroxyl groups that are generated via water dissociation at the Pt−O−Mo sites. The CO_2 product is thus formed, and the oxygen vacancies are regenerated around the interface, meaning that the WGS reaction is sustainable on the catalyst refined by Pt clusters. By contrast, the adsorption of CO on γ-Mo_2N support is much more difficult (Figure S20), which makes the reaction unable to continue once the surface hydroxyls are saturated. In addition to the easier CO adsorption (Figure S21, Table S4), interactions of the Pt clusters with hydrogen are sufficiently strong to grab the produced hydrogen atoms for subsequent H_2 generation via a reverse spillover process (Figure 7b); otherwise, the hydrogen atom would be captured by surface oxygen to form inactive hydroxyl groups. However, the strong interaction with hydrogen may lead to a high energy cost of H_2 desorption, which will hinder the water adsorption and the WGS reaction to some extent on Pt/γ-Mo_2N catalysts as aforementioned. We note in passing that the free energy cost for H_2 desorption in reality should be lower than the calculated value of 1.47 eV since the Pt clusters in the experiments are larger than the Pt_4 model used in the calculations and thereby contains surface Pt atoms with higher coordination numbers. Nevertheless, to further improve the performance of Pt/γ-Mo_2N catalysts, the challenge of lowering the desorption energy of H_2 still needs to be overcome, perhaps via modifying the Pt species with the addition of promoters such as alkali ions.

CONCLUSION

In summary, we have successfully developed a Pt/γ-Mo_2N catalyst, which demonstrated the highest specific reaction rate in the WGS reaction beyond all the reported catalysts, as well as impressive long-term stability. On account of the stress between the bulk γ-Mo_2N phase and surface oxide species, the formation of the highly distorted MoO_x species that is rich in oxygen vacancies has a large energy advantage in thermodynamics on the surface of the γ-Mo_2N support. During the reaction, the γ-Mo_2N support with surface MoO_x contributes vast active oxygen vacancies that can sustainably dissociate H_2O molecules to produce surface −OH groups to react with CO. Overall, the crucial role of the surface MoO_x in catalyzing the WGS reaction has been revealed for the Pt/γ-Mo_2N catalyst, which deepens the understanding of the effect of the heterostructured surface on the catalytic performance and provides a strategy to develop efficient heterogeneous catalysts.

ASSOCIATED CONTENT

Supporting Information

The Supporting Information is available free of charge at https://pubs.acs.org/doi/10.1021/jacs.9b11088.

Methods of simulation, experimental data, and additional discussion are displayed, containing catalytic reactivity, kinetic results, further characterization of the catalysts, and simulation details (PDF)

AUTHOR INFORMATION

Corresponding Authors

Chun-Jiang Jia − *Key Laboratory for Colloid and Interface Chemistry, Key Laboratory of Special Aggregated Materials, School of Chemistry and Chemical Engineering, Shandong University, Jinan 250100, China*; orcid.org/0000-0002-4254-5100; Email: jiacj@sdu.edu.cn

Rui Si − *Shanghai Synchrotron Radiation Facility, Shanghai Institute of Applied Physics, Chinese Academy of Sciences, Shanghai 201204, China*; Email: sirui@sinap.ac.cn

Chao Ma − *College of Materials Science and Engineering, Hunan University, Changsha 410082, China*; orcid.org/0000-0001-8599-9340; Email: cma@hnu.edu.cn

Authors

Zhe-Shan Zhang − *Key Laboratory for Colloid and Interface Chemistry, Key Laboratory of Special Aggregated Materials, School of Chemistry and Chemical Engineering, Shandong University, Jinan 250100, China*

Qiang Fu − *Key Laboratory for Colloid and Interface Chemistry, Key Laboratory of Special Aggregated Materials, School of*

Chemistry and Chemical Engineering, Shandong University, Jinan 250100, China; orcid.org/0000-0002-6682-8527

Kai Xu − *Key Laboratory for Colloid and Interface Chemistry, Key Laboratory of Special Aggregated Materials, School of Chemistry and Chemical Engineering, Shandong University, Jinan 250100, China*

Wei-Wei Wang − *Key Laboratory for Colloid and Interface Chemistry, Key Laboratory of Special Aggregated Materials, School of Chemistry and Chemical Engineering, Shandong University, Jinan 250100, China*

Xin-Pu Fu − *Key Laboratory for Colloid and Interface Chemistry, Key Laboratory of Special Aggregated Materials, School of Chemistry and Chemical Engineering, Shandong University, Jinan 250100, China*

Xu-Sheng Zheng − *National Synchrotron Radiation Laboratory, Department of Chemical Physics, University of Science and Technology of China, Hefei 230026, China*

Ke Wu − *Beijing National Laboratory for Molecular Sciences, State Key Lab of Rare Earth Materials Chemistry and Applications, PKU-HKU Joint Lab in Rare Earth Materials and Bioinorganic Chemistry, Peking University, Beijing 100871, China*

Ling-Dong Sun − *Beijing National Laboratory for Molecular Sciences, State Key Lab of Rare Earth Materials Chemistry and Applications, PKU-HKU Joint Lab in Rare Earth Materials and Bioinorganic Chemistry, Peking University, Beijing 100871, China*

Chun-Hua Yan − *Beijing National Laboratory for Molecular Sciences, State Key Lab of Rare Earth Materials Chemistry and Applications, PKU-HKU Joint Lab in Rare Earth Materials and Bioinorganic Chemistry, Peking University, Beijing 100871, China;* orcid.org/0000-0002-0581-2951

Complete contact information is available at: https://pubs.acs.org/10.1021/jacs.9b11088

Author Contributions

[#]Z.-S. Zhang and Q. Fu contributed equally.

Notes

The authors declare no competing financial interest.

■ ACKNOWLEDGMENTS

We are grateful for financial support from the Excellent Young Scientists Fund from the National Science Foundation of China (NSFC) (grant nos. 21622106), other projects from the NSFC (grant nos. 21331001, 21773288, 21771117, 21803036, and 21805167), the Outstanding Scholar Fund from the Science Foundation of Shandong Province of China (grant no. JQ201703), the Doctoral Fund from the Science Foundation of Shandong Province of China (grant no. ZR2018BB010), the Taishan Scholar Project of Shandong Province of China, the Shandong Provincial Natural Science Foundation, China (grant no. ZR2018QB005), and the Young Scholars Program of Shandong University (grant nos. 11190089964158 and 2018WLJH49). We thank the Center of Structural Characterizations and Property Measurements at Shandong University for the help on sample characterizations. First-principles calculations were performed on the HPC Cloud Platform of Shandong University.

■ REFERENCES

(1) Chen, M. S.; Goodman, D. W. The structure of catalytically active gold on titania. *Science* **2004**, *306*, 252−255.

(2) Cargnello, M.; Doan-Nguyen, V. V. T.; Gordon, T. R.; Diaz, R. E.; Stach, E. A.; Gorte, R. J.; Fornasiero, P.; Murray, C. B. Control of metal nanocrystal size reveals metal-support interface role for ceria catalysts. *Science* **2013**, *341*, 771−773.

(3) Qiao, B.; Wang, A.; Yang, X.; Allard, L. F.; Jiang, Z.; Cui, Y.; Liu, J.; Li, J.; Zhang, T. Single-atom catalysis of CO oxidation using Pt_1/FeO_x. *Nat. Chem.* **2011**, *3*, 634−64.

(4) Comotti, M.; Li, W.-C.; Spliethoff, B.; Schüth, F. Support effect in high activity gold catalysts for CO oxidation. *J. Am. Chem. Soc.* **2006**, *128*, 917−924.

(5) Wang, W.-W.; Yu, W.-Z.; Du, P.-P.; Xu, H.; Jin, Z.; Si, R.; Ma, C.; Shi, S.; Jia, C.-J.; Yan, C.-H. Crystal plane effect of ceria on supported copper oxide cluster catalyst for CO oxidation: importance of metal-support interaction. *ACS Catal.* **2017**, *7*, 1313−1329.

(6) Fu, Q.; Saltsburg, H.; Flytzani-Stephanopoulos, M. Active nonmetallic Au and Pt species on ceria-based water-gas shift catalysts. *Science* **2003**, *301*, 935−938.

(7) Zhai, Y.; Pierre, D.; Si, R.; Deng, W.; Ferrin, P.; Nilekar, A. U.; Peng, G.; Herron, J. A.; Bell, D. C.; Saltsburg, H.; Mavrikakis, M.; Flytzani-Stephanopoulos, M. Alkali-stabilized Pt-OH_x species catalyze low-temperature water-gas shift reactions. *Science* **2010**, *329*, 1633−1636.

(8) Yang, M.; Li, S.; Wang, Y.; Herron, J. A.; Xu, Y.; Allard, L. F.; Lee, S.; Huang, J.; Mavrikakis, M.; Flytzani-Stephanopoulos, M. Catalytically active Au-O$(OH)_x$-species stabilized by alkali ions on zeolites and mesoporous oxides. *Science* **2014**, *346*, 1498−1501.

(9) Schweitzer, N. M.; Schaidle, J. A.; Ezekoye, O. K.; Pan, X.; Linic, S.; Thompson, L. T. High activity carbide supported catalysts for water gas shift. *J. Am. Chem. Soc.* **2011**, *133*, 2378−2381.

(10) Patt, J.; Moon, D. J.; Phillips, C.; Thompson, L. Molybdenum carbide catalysts for water-gas shift. *Catal. Lett.* **2000**, *65*, 193−195.

(11) Yao, S.; Zhang, X.; Zhou, W.; Gao, R.; Xu, W.; Ye, Y.; Lin, L.; Wen, X.; Liu, P.; Chen, B.; Crumlin, E.; Guo, J.; Zuo, Z.; Li, W.; Xie, J.; Lu, L.; Kiely, C. J.; Gu, L.; Shi, C.; Rodriguez, J. A.; Ma, D. Atomic-layered Au clusters on α-MoC as catalysts for the low-temperature water-gas shift reaction. *Science* **2017**, *357*, 389−393.

(12) McGee, R. C. V.; Bej, S. K.; Thompson, L. T. Basic properties of molybdenum and tungsten nitride catalysts. *Appl. Catal., A* **2005**, *284*, 139−146.

(13) Karunadasa, H. I.; Montalvo, E.; Sun, Y.; Majda, M.; Long, J. R.; Chang, C. J A molecular MoS_2 edge site mimic for catalytic hydrogen generation. *Science* **2012**, *335*, 698−702.

(14) Kropp, T.; Paier, J.; Sauer, J. Support effect in oxide catalysis: methanol oxidation on vanadia/ceria. *J. Am. Chem. Soc.* **2014**, *136*, 14616−14625.

(15) Karim, W.; Spreafico, C.; Kleibert, A.; Gobrecht, J.; VandeVondele, J.; Ekinci, Y.; van Bokhoven, J. A. Catalyst support effects on hydrogen spillover. *Nature* **2017**, *541*, 68−71.

(16) Szeto, K. C.; Jones, Z. R.; Merle, N.; Rios, C.; Gallo, A.; Le Quemener, F.; Delevoye, L.; Gauvin, R. M.; Scott, S. L.; Taoufik, M. A strong support effect in selective propane dehydrogenation catalyzed by Ga$(i\text{-Bu})_3$ grafted onto -alumina and silica. *ACS Catal.* **2018**, *8*, 7566−757.

(17) Si, R.; Flytzani-Stephanopoulos, M. Shape and crystal-plane effects of nanoscale ceria on the activity of Au-CeO_2 catalysts for the water-gas shift reaction. *Angew. Chem., Int. Ed.* **2008**, *47*, 2884−2887.

(18) Giordano, C.; Antonietti, M. Synthesis of crystalline metal nitride and metal carbide nanostructures by sol-gel chemistry. *Nano Today* **2011**, *6*, 366−380.

(19) Yang, C.; Zhao, H.; Hou, Y.; Ma, D. Fe_5C_2 Nanoparticles: A Facile Bromide-Induced Synthesis and as an Active Phase for Fischer−Tropsch Synthesis. *J. Am. Chem. Soc.* **2012**, *134*, 15814−15821.

(20) Schaidle, J. A.; Thompson, L. T. Fischer−Tropsch synthesis over early transition metal carbides and nitrides: CO activation and chain growth. *J. Catal.* **2015**, *329*, 325−334.

(21) O'Neill, B. J.; Jackson, D. H. K.; Lee, J.; Canlas, C.; Stair, P. C.; Marshall, C. L.; Elam, J. W.; Kuech, T. F.; Dumesic, J. A.; Huber, G.

W. Catalyst design with atomic layer deposition. *ACS Catal.* **2015**, *5*, 1804−1825.

(22) Graciani, J.; Sanz, J. F. Designing a new generation of catalysts: Water gas shift reaction example. *Catal. Today* **2015**, *240*, 214−219.

(23) Ratnasamy, C.; Wagner, J. P. Water gas shift catalysis. *Catal. Rev.: Sci. Eng.* **2009**, *51*, 325−440.

(24) LeValley, T. L.; Richard, A. R.; Fan, M. The progress in water gas shift and steam reforming hydrogen production technologies-A review. *Int. J. Hydrogen Energy* **2014**, *39*, 16983−17000.

(25) Vecchietti, J.; Bonivardi, A.; Xu, W.; Stacchiola, D.; Delgado, J. J.; Calatayud, M.; Collins, S. E. Understanding the role of oxygen vacancies in the water gas shift reaction on ceria-supported platinum catalysts. *ACS Catal.* **2014**, *4*, 2088−2096.

(26) Kalamaras, C. M.; Americanou, S.; Efstathiou, A. M. Redox" vs "associative formate with-OH group regeneration" WGS reaction mechanism on Pt/CeO_2: Effect of platinum particle size. *J. Catal.* **2011**, *279*, 287−300.

(27) Kalamaras, C. M.; Panagiotopoulou, P.; Kondarides, D. I.; Efstathiou, A. M. Kinetic and mechanistic studies of the water-gas shift reaction on Pt/TiO_2 catalyst. *J. Catal.* **2009**, *264*, 117−129.

(28) Fu, X.-P.; Guo, L.-W.; Wang, W.-W.; Ma, C.; Jia, C.-J.; Wu, K.; Si, R.; Sun, L.-D.; Yan, C.-H Direct identification of active surface species for the water-gas shift reaction on a gold-ceria catalyst. *J. Am. Chem. Soc.* **2019**, *141*, 4613−4623.

(29) York, A. P. E.; Claridge, J. B.; Brungs, A. J.; Tsang, S. C.; Green, M. L. H. Molybdenum and tungsten carbides as catalysts for the conversion of methane to synthesis gas using stoichiometric feedstocks. *Chem. Commun.* **1997**, *1*, 39−40.

(30) Claridge, J. B.; York, A. P. E.; Brungs, A. J.; Marquez-Alvarez, C.; Sloan, J.; Tsang, S. C.; Green, M. L. H. New catalysts for the conversion of methane to synthesis gas: Molybdenum and tungsten carbide. *J. Catal.* **1998**, *180*, 85−100.

(31) Tsukazaki, A.; Ohtomo, A.; Kita, T.; Ohno, Y.; Ohno, H.; Kawasaki, M. Quantum Hall effect in polar oxide heterostructures. *Science* **2007**, *315*, 1388−1391.

(32) Tian, J.; Zhao, Z.; Kumar, A.; Boughton, R. I.; Liu, H. Recent progress in design, synthesis, and applications of one-dimensional TiO_2 nanostructured surface heterostructures: a review. *Chem. Soc. Rev.* **2014**, *43*, 6920−6937.

(33) O'Sullivan, M.; Hadermann, J.; Dyer, M. S.; Turner, S.; Alaria, J.; Manning, T. D.; Abakumov, A. M.; Claridge, J. B.; Rosseinsky, M. J. Interface control by chemical and dimensional matching in an oxide heterostructure. *Nat. Chem.* **2016**, *8*, 347−353.

(34) Zhou, P.; Xu, Q.; Li, H.; Wang, Y.; Yan, B.; Zhou, Y.; Chen, J.; Zhang, J.; Wang, K. Fabrication of two-dimensional lateral heterostructures of WS_2 /$WO_3{\cdot}H_2O$ through selective oxidation of monolayer WS_2. *Angew. Chem., Int. Ed.* **2015**, *54*, 15226−15230.

(35) Liu, P.; Rodriguez, J. A. Water-gas-shift reaction on molybdenum carbide surfaces: essential role of the oxycarbide. *J. Phys. Chem. B* **2006**, *110*, 19418−19425.

(36) Zheng, W.; Cotter, T. P.; Kaghazchi, P.; Jacob, T.; Frank, B.; Schlichte, K.; Zhang, W.; Su, D. S.; Schuth, F.; Schlogl, R. Experimental and theoretical investigation of molybdenum carbide and nitride as catalysts for ammonia decomposition. *J. Am. Chem. Soc.* **2013**, *135*, 3458−3464.

(37) Setthapun, W.; Bej, S. K.; Thompson, L. T. Carbide and nitride supported methanol steam reforming catalysts: Parallel synthesis and high throughput screening. *Top. Catal.* **2008**, *49*, 73−80.

(38) Li, G. R.; Song, J.; Pan, G. L.; Gao, X. P. Highly Pt-like electrocatalytic activity of transition metal nitrides for dye-sensitized solar cells. *Energy Environ. Sci.* **2011**, *4*, 1680−1683.

(39) Jaf, Z. N.; Altarawneh, M.; Miran, H. A.; Jiang, Z.-T.; Dlugogorski, B. Z. Mechanisms governing selective hydrogenation of acetylene over a-Mo_2N surfaces. *Catal. Sci. Technol.* **2017**, *7*, 943−960.

(40) Xu, W.; Zhao, K.; Wang, Y. Electrochemical activated MoO_2/Mo_2N heterostructured nanobelts as superior zinc rechargeable battery cathode. *Energy Storage Mater.* **2018**, *15*, 374−379.

(41) Camacho-López, M. A.; Escobar-Alarcón, L.; Picquart, M.; Arroyo, R.; Córdoba, G.; Haro-Poniatowski, E. Micro-Raman study of the m-MoO_2 to α-MoO_3 transformation induced by cw-laser irradiation. *Opt. Mater.* **2011**, *33*, 480−484.

(42) Tan, X.; Wang, L.; Cheng, C.; Yan, X.; Shen, B.; Zhang, J. Plasmonic MoO_{3-x}@MoO_3 nanosheets for highly sensitive SERS detection through nanoshell-isolated electromagnetic enhancement. *Chem. Commun.* **2016**, *52*, 2893−2896.

(43) Li, Z.; Li, Y.; Zhan, E.; Ta, N.; Shen, W. Morphology-controlled synthesis of h-MoO_3 nanomaterials for ethanol oxidation. *J. Mater. Chem. A* **2013**, *1*, 15370−15376.

(44) Li, C.; Shao, Z.; Pang, M.; Williams, C. T.; Liang, C. Carbon nanotubes supported Pt catalysts for phenylacetylene hydrogenation: effects of oxygen containing surface groups on Pt dispersion and catalytic performance. *Catal. Today* **2012**, *186*, 69−75.